DOI 10.24425/aee.2025.154992

# Investigation and analysis of torque generation mechanism of reverse salient permanent magnet synchronous machine

XIPING LIU, JIAO GUO DE ZHANGQI LIU, BAOYU SUN

School of Electrical Engineering and Automation, Jiangxi University of Science and Technology No. 1958, Kejia Road, Ganzhou, People's Republic of China

*e-mail:* ⋈ *Jiao Guo1655663491@qq.com* 

(Received: 08.04.2025, revised: 25.08.2025)

Abstract: In this paper, the torque generation mechanism of the reverse salient permanent magnet synchronous machine (RSPMSM) is investigated. The magnetic equivalent circuit (MEC) and the equivalent reluctance of different magnetic circuits are used to determine the air-gap magnetic density without slotting. By incorporating the influence of the slotted Carter factor, a model for the air-gap magnetic density at no-load is deduced and compared to finite element analysis results. The strong agreement observed between the analytical method and finite element analysis validates the precision of the proposed methodology. Moreover, the Maxwell stress method is employed to analyze and demonstrate the generation mechanism of electromagnetic torque. The contributions of the fundamental wave and each order harmonic to the torque components and their proportions are determined. This analysis provides valuable insights into the generation process of torque in the machine. Additional prototype experiments were conducted to verify the validity of the theoretical analysis and finite element simulations. The experimental results further confirm the accuracy and validity of the proposed methodologies.

**Key words:** air-gap magnetic density, analytical method, magnetic equivalent circuit (MEC), magnetic field modulation effect, torque quantitative analysis

# 1. Introduction

Permanent magnet synchronous machines (PMSMs) have attracted the attention of many experts and scholars at home and abroad due to the simple structure, high power density, high efficiency, and high reliability [1–3], and have become one of the commonly used drive motor types



© 2025. The Author(s). This is an open-access article distributed under the terms of the Creative Commons Attribution-NonCommercial-NoDerivatives License (CC BY-NC-ND 4.0, https://creativecommons.org/licenses/by-nc-nd/4.0/), which permits use, distribution, and reproduction in any medium, provided that the Article is properly cited, the use is non-commercial, and no modifications or adaptations are made.

for electric vehicles [4]. However, the structure of PMSMs is changeable [5] and the magnetic field distribution is complex [6], accurate analysis of the harmonic distribution of the air-gap magnetic field of the PMSM and complete consideration of various factors affecting the air-gap magnetic field distribution are the key to the motor design and the optimization of electromagnetic performance.

Common methods for analyzing the electromagnetic field of motors include the magnetic equivalent circuit (MEC) [7–11], the subdomain method (SD) [12–16], and the finite element method (FEM) [7-21], which have been studied by many scholars both domestically and internationally. A MEC method for analyzing the magnetic flux density of the air gap considering the multi-segmented and multi-layered is proposed in [7], which takes into account the grooving effect in the lower part of the tooth and the flux concentration in the lower part of the tooth. An analytical model of the V-shaped segmented skewed poles IPMSM air-gap magnetic field is established in [8] by combining subdomain method and MEC method. Then the analytical model is obtained by introducing the complex relative permeance. In [9], an analytical model based on magnetic equivalent circuit (MEC) method is proposed. The analytical model can provide radial and tangential components by combining the boundary conditions of macroscopic equations B and H in magnetostatics. A hybrid subdomain and equivalent magnetic circuit model is proposed in [13], which uses the current distribution in the SD model on the surface of modulators and rotor core, as well as in the stator slots, and calculates the saturation current density in combination with the MEC model. A hybrid subdomain model accounting for slotting effect, rotor saliency, and iron nonlinearity is proposed in [14] for magnetic field analysis. A two-dimensional hybrid analytical model in polar coordinate system is proposed in [15] by combining two-dimensional exact subdomain technology and magnetic equivalent circuit technology for the calculation of magnetic field under no-load and rated-load conditions of dual-rotor PM synchronous machines. A new type of double-layer V-type permanent magnet machine is proposed in [19], and its basic electromagnetic properties are evaluated by finite element simulation and compared with a Nissan Leaf IPM machine. In [20], the finite element simulation is used to obtain the electromagnetic characteristics of switched flux PMSM under no-load and rated loads, and the generation mechanism of torque is analyzed. Above all, the MEC is mostly used to study and derive the air-gap magnetic density of motors with simple magnetic circuits, while the SD will lead to complex modeling and solving processes, and the FEM must rely on multiple finite element models.

Conventional IPMSM have the risk of PM demagnetization when the electromagnetic field is weakened [22]. To address this shortcoming, Bianchi et al. first innovatively proposed the concept of Reverse Salient Permanent Magnet Synchronous Motor (RSPMSM) [23]. Compared with the traditional V-type IPMSM, the d-axis inductance  $L_d$  of the RSPMSM is greater than the q-axis inductance  $L_q$  [24]. The flux-intensifying effect can reduce the flux-weakening current and widen the speed range [25]. The RSPMSM can reduce the risk of demagnetization of PMs, but there is lower torque density than the conventional V-shaped IPMSM [26].

Most of the existing studies on RSPMSMs are based on the analysis of electromagnetic performance [27–30]. The analytical modeling and optimization techniques of RSPMSM are mainly for the design of the magnetic flux leakage path of the motor to achieve better performance in [28] and [29]. It focuses on the design and performance comparison of leakage flux paths, while there is less research on the deeper principles of air-gap magnetic field and torque generation, ignoring the internal air-gap magnetic field modulation mechanism brought on different rotor structures. The common methods used to calculate the electromagnetic field of RSPMSM (i.e., MEC and SD) are not accurate, since the magnetic circuit structure of RSPMSM is complex. To

gain a deeper understanding of the torque generation mechanism, the modified MEC method is used to derive and verify the reluctance of each magnetic circuit and the no-load air-gap magnetic density of the RSPMSM with complex magnetic barrier in this paper. The torque of RSPMSM is analyzed, and the contribution of fundamental wave and harmonics to the torque components is determined. It focuses on obtaining torque through the theoretical analysis of the air-gap magnetic field and reveals the theoretical basis of torque in RSPMSM from the perspective of identifying and quantifying the harmonic torque contribution of the air-gap magnetic field.

In this paper, the torque generation mechanism of the RSPMSM is investigated and the torque components provided by the harmonics of each order are quantitatively analyzed. The paper is organized as follows: Section 2 presents two RSPMSM topologies and the analysis of their demagnetization stability. Section 3 performs some experimental measurements on the RSPMSM prototype to validate the finite element method. Section 4 gives a comparison of the analytical model of the no-load air-gap magnetic field with the finite element method, where the equivalence of the reluctance and the effect of stator slotting are considered, and the magnitude of each harmonic is derived and the contribution of each order of harmonic to the torque is quantified. Conclusions are given in Section 5.

### 2. Machine topologies

Due to the risk of demagnetization of conventional V-shape Interior Permanent Magnet motors (IPM), two RSPMSMs with high demagnetization stability are considered in this paper as shown in Fig. 1. Table 1 shows the main design parameters of two RSPMSMs. Both machines have the same stator configuration, with double-layer distributed windings connected in a Y-type manner. The structure of the rotor is different. The RSPMSM I adopt arc-shaped PMs and sector magnetic barriers. And the arc-shaped magnetic barriers are designed at the *q*-axis of rotor to modify the magnetic flux path. RSPMSM II adopts the traditional V-shaped PM with bowl-shaped and arc-shaped magnetic barriers on the *q*-axis of rotor. And the RSPMSM II incorporates three layers of parallel magnetic barriers to mitigate strong cross-coupling magnetic saturation between the *d*-axis and the *q*-axis. Furthermore, to perform a fair comparison, the two RSPMSMs share the same air-gap length, axial length, and current density. Detailed structures are depicted in Fig. 1(a) and Fig. 1(b), respectively.

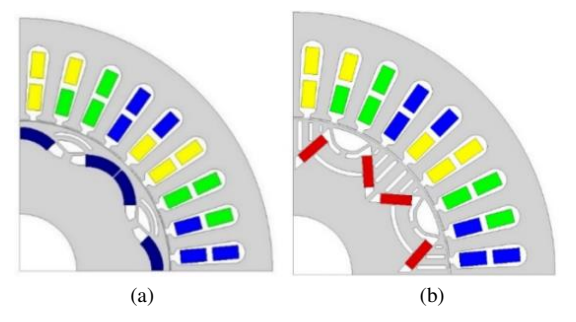


Fig. 1. 1/4 RSPMSM model: (a) RSPMSM I (Arc-shaped PM); (b) RSPMSM II (V-shaped PM)

Table 1. Structural parameter

Parameters	RSPMSM I	RSPMSM II	
Number of phases	3 phases		
Number of poles/slots	8/36		
Rated output power	2.5 kW		
Rated current	13.67 A		
Rated speed	1 500 r/min		
Stator outer diameter	155 mm		
Stator inner diameter	93 mm		
Rotor outer diameter	92 mm		
Rotor inner diameter	35 mm		
The axial length of the motor	70 mm		
Pitch	4		
Number of turns	13		
PM shape	Arc-shaped V-shaped		
PM grade	N42SH		

The finite element analysis in this paper is done in the software ANSYS Electronics 2021. The basic modeling information is shown in Table 2. It is worth noting that the mesh density of the air gap is set to be minimized more accurately because of the higher accuracy required for the air gap. The stator and rotor are made of DW310-35 material, which has good magnetic properties and low iron loss. The permanent magnets are made of N42SH, a material with high magnetic energy product.

Table 2. Basic finite element modeling information

Main motor	Mesh density	Materials	Boundary conditions	Solving setup	
components	(mm)	17440011415	201111111111111111111111111111111111111	time	step
Stator	3	DW310-35		4T (period)	T/50
Rotor	3	DW310-35	Master-slave boundary		
Permanent magnet	2	N42SH	conditions for permanent magnet motors	Backward Euler method	
Air gap	1	Air			
Coil	2.5	copper			

In order to verify the demagnetization stability of the two motors, the observation points on the PM of the conventional V-type IPMSM and the two RSPMSMs are selected for analysis. At rated load, the d-axis currents are -7.8 A, 0.8 A, and 1.2 A. The flux density distributions of the conventional V-type IPMSM and the two RSPMSMs are shown in Fig. 2. Comparing the PM flux densities of the conventional IPMSM and the two RSPMSMs, it can be seen that the overall flux densities of the two RSPMSMs are higher than that of the conventional V-type IPMSM. The centerlines  $B_1$ ,  $B_2$  and  $B_3$  are selected as the observation points, and the variation of the PM densities at the observation points is shown in Fig. 3(a). It can be seen that the magnetic densities of the three observation points are all greater than 1 T. The flux density variations of the observation points in the weak magnetic state are shown in Fig. 3(b). Compared with the magnetic density under the rated load, the magnetic density of the PM decreases under the weak magnetic current, but the magnetic density of RSPMSM I is always higher than that of RSPMSM II, and the magnetic field of the higher magnetic density can be weakened by the smaller Id, which reduces the risk of demagnetization of the PM generator.

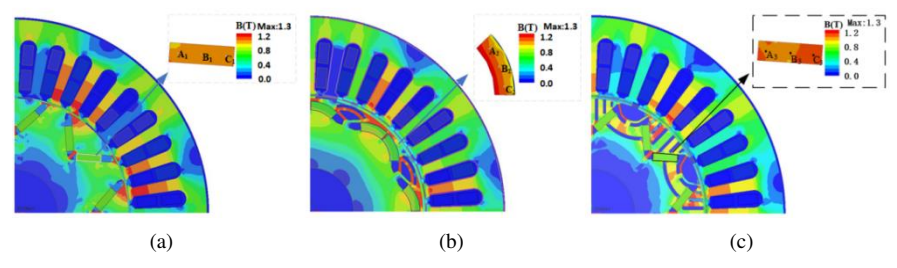


Fig. 2. Magnetically dense distribution under rated working conditions: (a) conventional V-shaped IPMSM; (b) RMSMPM I; (c) RMSMPM II

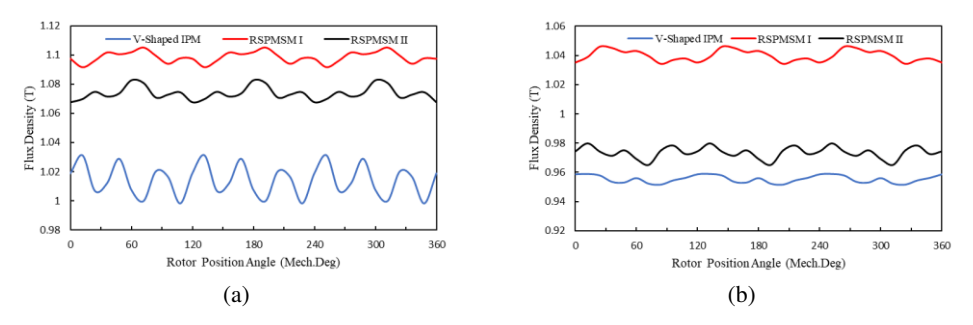
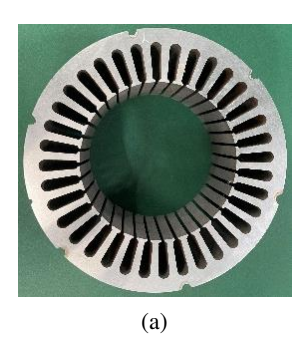


Fig. 3. Magnetic density of PM observation points: (a) rated load (1500 rpm); (b) high-speed weak field condition (5000 rpm)

# 3. Experimental validation of FEM model

In order to verify the above theoretical analyses and finite element, a prototype of arc-shaped PM is manufactured. The stator and rotor of the prototype are shown in Fig. 4(a) and Fig. 4(b), respectively.



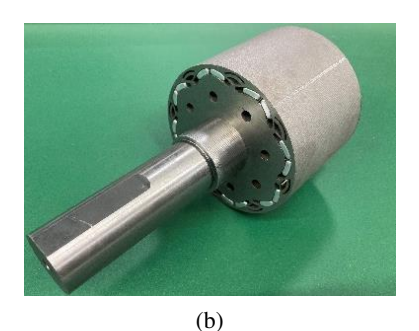


Fig. 4. Prototype of RSPMSM I: (a) stator; (b) rotor

The test platform is built to test the no-load back-EMF, as shown in Fig. 5. The no-load back-EMFs of the machine prototype with rated speed of 1500 r/min and can be measured by the test platform. The finite element results and the prototype experimental results of no-load back-EMF are shown in Fig. 6(a). The simulated waveform amplitude is 59.1 V, and the test value is 62.5 V, the difference between the two waveforms is small, and the error value is 5.7%. By comparing the measured waveform with the waveform predicted by finite element, and the magnitude of the error value, it can be seen that the waveform is in good agreement. Due to the error of the process technology during the machining of the motor, the test results are larger than the simulation results, but within the acceptable range. The no-load back-EMF test results of the motor at 3000 rpm are obtained by changing the rotational speed, as shown in Fig. 6(b). Comparison with the simulation results shows that the phase no-load back-EMF amplitude obtained from the experimental test is 125.8 V, which is slightly larger than the simulation amplitude of 117.8 V, with better sinusoidal properties. However, it cannot be denied that the FEM simulation results show higher harmonic content compared to experimental measurements. This difference is mainly caused by the filtering effect of iron core loss and rotor eddy current phenomenon.

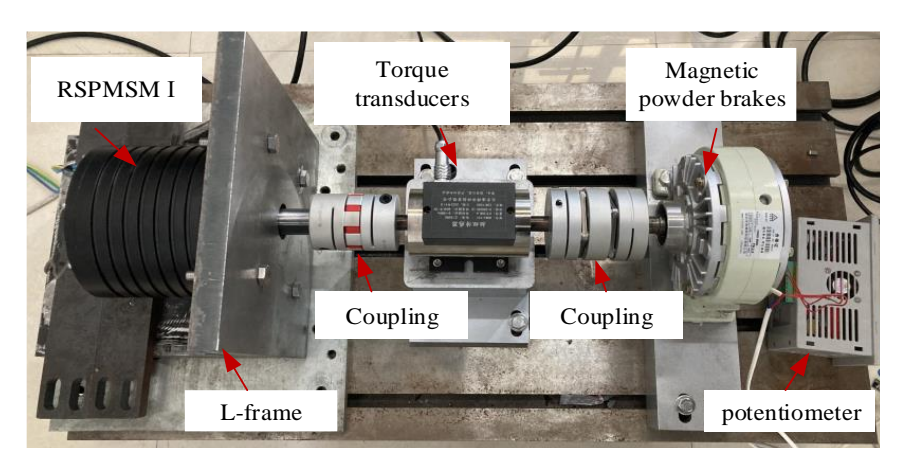


Fig. 5. Test platform

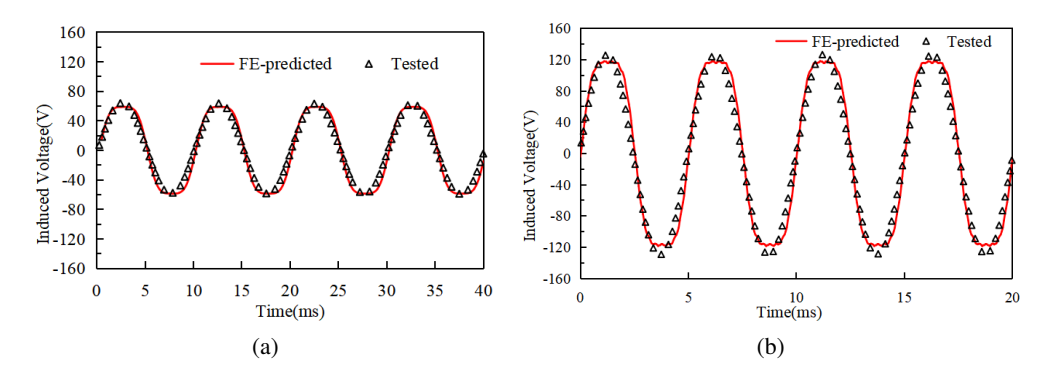


Fig. 6. Comparison of the measured and FE-predicted open-circuit back-EMFs at different RPMs: (a) 1500 r/min; (b) 3000 r/min

Figure 7 shows the current waveforms of the d-axis and q-axis of RSPMSM I under different loads.  $I_d$  of RSPMSM I changed from -0.43 A to 1.3 A, while  $I_q$  increased from 1.25 A to 8.2 A. It can be seen that Id changes from negative to positive under different load conditions, which is negative at low load and greater than zero when high load is applied.

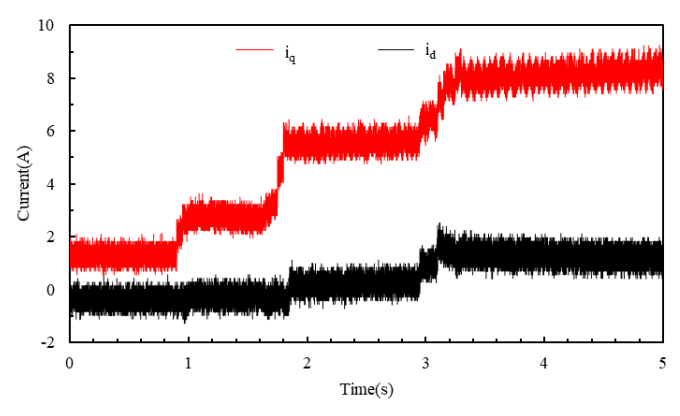


Fig. 7. Currents of d-axis and q-axis under different loads

In order to further verify the accuracy of the model under different working conditions, varying load testing are carried out on the RSPMSM, as shown in Fig. 8. The load of the magnetic power brakes data is obtained and sampled to the host computer for export, resulting in no torque ripple in the torque waveform shown in Fig. 8(a). Nevertheless, it can be seen from Fig. 8(a) that as the load torque varies from -0.2 Nm to -4 Nm, the corresponding phase current varies from 0.8 A to 5.2 A, as shown in Fig. 8(b). At a load of -2.2 Nm, the phase current is zoomed. It can be found the current is approximately sinusoidal, which provides good performance when the motor speed is set to 1500 r/min.

The above series of results show that the finite element simulation is highly consistent with the test results, which verifies the correctness of the theoretical analysis.

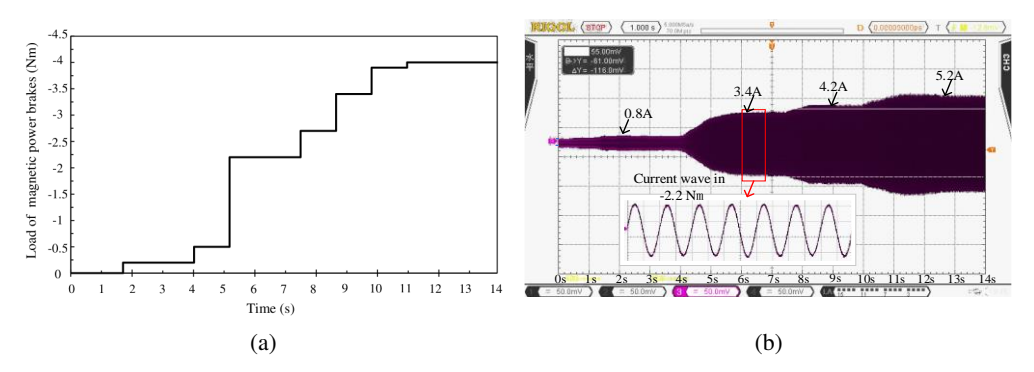


Fig. 8. Varying load testing at 1500 r/min: (a) load of magnetic power brakes; (b) current waveform

# 4. Comparison of analytical methods and finite element analysis

### 4.1. Model of the no-load air-gap magnetic field

The magnetic field distributions of the two RSPMSMs are shown in Fig. 9. The maximum value of magnetic density at the magnetic bridge. The PMs of RSPMSM I is arc-shaped and the direction of magnetization is axial, resulting in more magnetic flux leakage in RSPMSM I than RSPMSM II. Therefore, in Fig. 9, the average rotor magnetic field of RSPMSM I is higher than that of RSPMSM II, and the average stator magnetic field is lower than that of RSPMSM II. According to the special structure of the RSPMSM, the magnetic circuit can be obtained, as shown in Fig. 10. In Fig. 10(a), magnetic circuit 1 represents the main magnetic flux in RSPMSM I. The magnetic flux generated by the PM passes through the rotor and the air gap, ultimately reaching the stator to produce electromagnetic torque. Magnetic circuits 2, 3, and 4 correspond to the leakage magnetic circuits. Here, the magnetic flux generated by the PM is altered by the presence of air magnetic barriers in the rotor and is redirected along the magnetic bridge towards the opposite side of the PM. The analytical modeling of the magnetic field in RSPMSM is derived based on the following assumptions.

- 1. Ignore the core saturation phenomenon.
- 2. Ignore the influence of armature winding.
- 3. The eccentricity and vibration of the rotor are not considered.

The reluctance of the stator and rotor in the magnetic circuit is much smaller than that of the air gap, hence it can be overlooked. In RSPMSM II, the presence of parallel magnetic barriers on both sides of the d-axis magnetic circuit primarily affects the accumulation of magnetic flux density in the barrier region but have little effect on the total magnetic flux passing through the air gap. Hence, the parallel magnetic barriers can be initially disregarded. Figure 11 illustrates the magnetic equivalent circuits for RSPMSM I and RSPMSM II. In Fig. 11(a),  $\Phi_g$  is the main magnetic flux of the air gap,  $\Phi_m$  is the total flux generated by the PM,  $\Phi_r$  is the magnetic flux inside the PMs,  $R_g$  is the reluctance of the air gap,  $R_{mo}$  is the reluctance of the PM, and  $R_{c1}$ ,  $R_{c2}$ , and  $R_{c3}$  are the magnetic flux leakage equivalent reluctance between adjacent PMs,where  $R_{c1}$ ,  $R_{c2}$  and  $R_{c3}$  are assumed to be the equivalent reluctances of the corresponding magnetic circuits 2, 3 and 4 in Fig. 10, respectively.

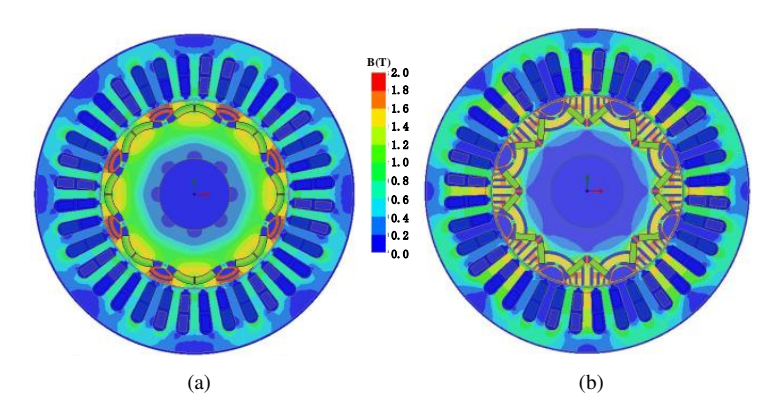


Fig. 9. Magnetic field distributions of RSPMSM: (a) RSPMSM I; (b) RSPMSM II

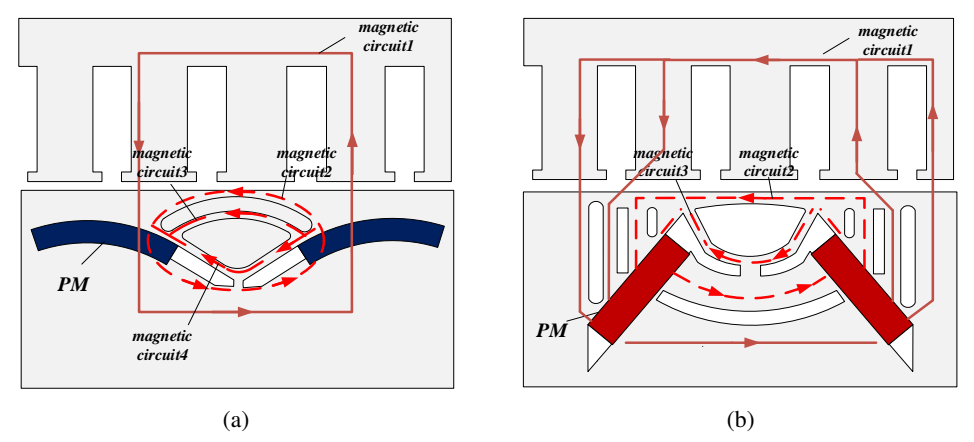


Fig. 10. Magnetic circuit diagram: (a) RSPMSM I; (b) RSPMSM II

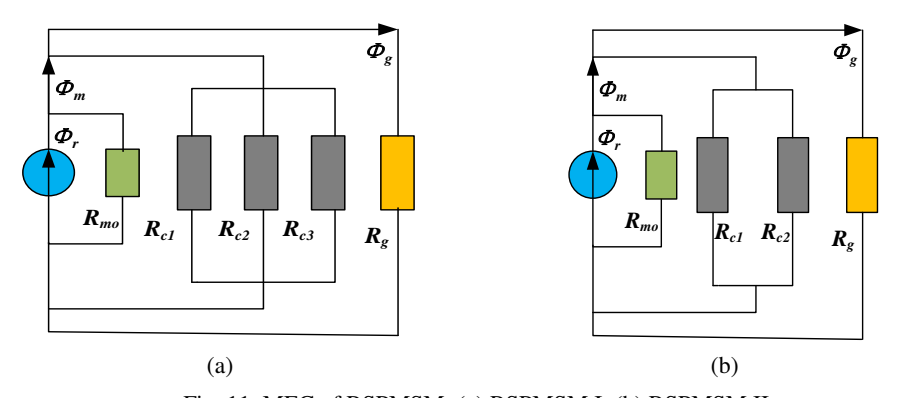


Fig. 11. MEC of RSPMSM: (a) RSPMSM I; (b) RSPMSM II

The reluctance of PM can be obtained according to the following equation [31]:

$$R_{m0} = \frac{h_{pm}}{\mu_0 \mu_m A_m},\tag{1}$$

where  $\mu_0$  is the vacuum permeability,  $\mu_m$  is the relative permeability of the PM material, and  $A_m$  is the area through which the magnetic flux of the permanent magnet passes.

$$A_m = \left(\frac{h_{pm}}{2} + r_{mi}\right) \theta_r l_{ar}.$$

 $r_{mi}$  is the radius of the arc-shaped PM, and  $\theta_r$  is the central angle of the arc-shaped PM. In RSPMSM II,  $A_m = l_{pm}l_{ar}$ , where  $l_{pm}$  and  $l_{ar}$  are the length of the PM and air gap. The air-gap reluctance of the RSPMSM is:

$$R_g = \frac{g_e}{\mu_0 A_g},\tag{2}$$

where  $g_e$  is the width of the air-gap, and  $A_g$  is the area through which the magnetic flux of the air gap passes.

$$A_g = \left(\frac{g_e}{2} + r_{ro}\right) \theta_m l_{ar},$$

where  $r_{ro}$  is the outer radius of the rotor and  $\theta_m = \frac{\pi}{n}$ .

Magnetic barriers affect the magnetic density of the air gap. When calculating the reluctance of magnetic circuit 2, magnetic circuit 3 and magnetic circuit 4, it is necessary to consider the change in reluctance caused by the change of magnetic circuit caused by magnetic barrier. From the magnetic circuit in Fig. 10, the magnetic circuit 2 in the RSPMSM I can be equivalent to the superposition of two trapezoidal magnetic circuits, the magnetic circuit 3 can be equivalent to a section of arc-shaped magnetic circuit, and the magnetic circuit 4 can be equivalent to a V-shaped magnetic circuit, and the specific shapes and dimensions are shown in Fig. 12. The magnetic circuit 2 in RSPMSM II is equivalent to an arc-shaped magnetic circuit, and the magnetic circuit 3 can be equivalent to the superposition of an arc-shaped magnetic circuit and two rectangular magnetic circuits, and the specific shapes and dimensions are shown in Fig. 13.

According to Fig. 11, the reluctance of each leakage magnetic circuit in the RSPMSM I can be deduced as follows:

$$R_{c1} = \frac{2 * h_1}{\mu_0 \mu_r l_{ar} (w_{t1} - w_{c1})} \ln \frac{w_{t1}}{w_{c1}},\tag{3}$$

$$R_{c2} = \frac{\theta_2}{\mu_0 \mu_r \ln \frac{r_o}{r_i}},\tag{4}$$

$$R_{c3} = \frac{h_{i3} + h_{o3}}{\mu_0 \mu_r l_{ar} w_3},\tag{5}$$

where  $\mu_r$  is the relative permeability of the rotor,  $l_{ar}$  is the axial length of the motor. According to the MEC, the air-gap flux  $\Phi_g$  can be calculated, which is expressed as:

$$\Phi_g = \frac{R_{mo}R_c}{(R_{mo} + R_{cg})(R_g + R_c)}\Phi_r,$$
(6)

where

$$R_c = \frac{1}{\left(\frac{1}{R_{c1}} + \frac{1}{R_{c2}} + \frac{1}{R_{c3}}\right)}, \quad R_{cg} = \frac{1}{\left(\frac{1}{R_c} + \frac{1}{R_g}\right)}, \quad \Phi_r = B_r A_m.$$

 $B_r$  is the remanence coefficient. According to the magnetic network theory, without considering the stator slot effect, the equivalent slot less air gap magnetic density [32] of the RSPMSM is shown in Fig. 14, and the mathematical model of the air-gap magnetic field is constructed by combining various reluctances. In Fig. 14,  $b = \theta_r \frac{B_s A_l}{(B_r A_m)}$ ,  $B_s$  is the magnetic flux density when the stator core is saturated,  $A_l$  is the magnetic flux area of magnetic flux leakage.

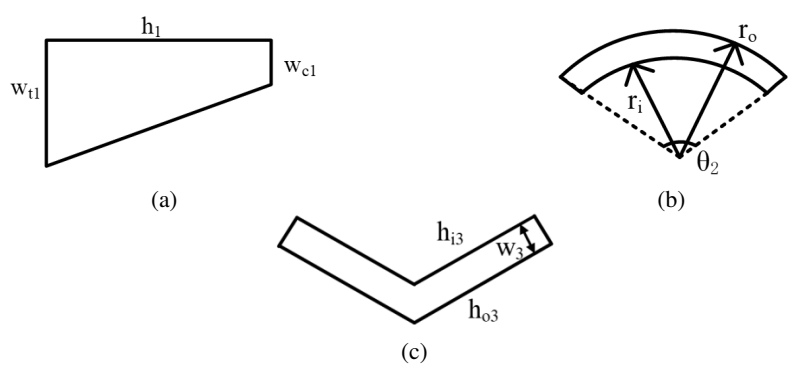


Fig. 12. MEC model of magnetic flux leakage branch in RSPMSM I: (a) magnetic circuit 2; (b) magnetic circuit 3; (c) magnetic circuit 4

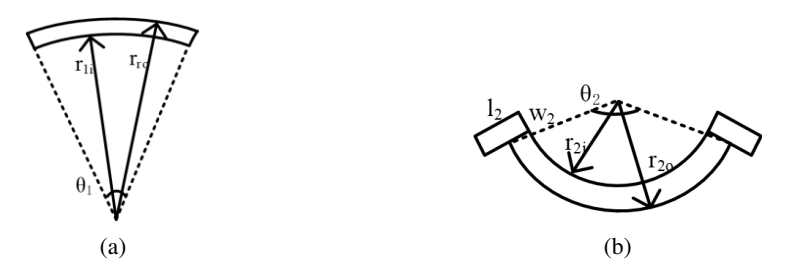


Fig. 13. MEC model of magnetic flux leakage branch in RSPMSM II; (a) magnetic circuit 2; (b) magnetic circuit 3

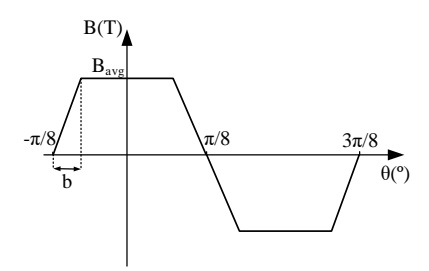


Fig. 14. Equivalent air-gap flux density of slotless

The average air-gap magnetic density of the RSPMSM can be expressed as:

$$B_{\text{avg}} = \frac{\Phi_g}{A_g} = \frac{R_{mo}R_c}{(R_{mo} + R_{cg})(R_g + R_c)} * \frac{B_r A_m}{A_g}.$$
 (7)

In the form of a Fourier series expansion, it can be expressed as:

$$B_g(\theta) = \sum_{\nu=1,3,5...} \frac{4B_{\text{avg}}}{\pi p b} \frac{\sin(\nu p b)}{\nu^2} \cos(\nu p \theta) = \sum_{\nu=1,3,5...} B_{\nu} \cos(\nu p \theta).$$
 (8)

The magnetic density under one pole pair as a function of the rotor angle is obtained by using MATLAB to calculate the magnetic density of the air gap, as shown in Fig. 15.

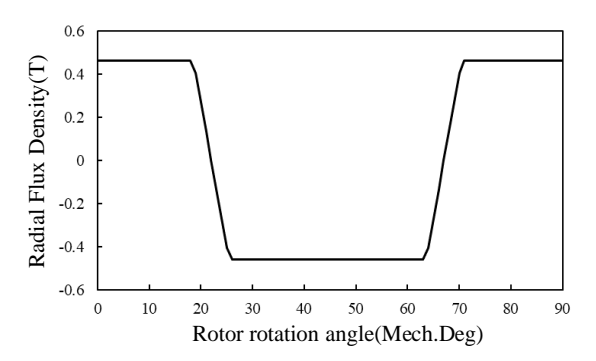


Fig. 15. Air-gap flux density under one pole pair

Stator slotting will change the equivalent air-gap length, which in turn affects the air gap permeability function. The Carter Factor is added to correct it when considering the effect of stator slotting. Since the length of the magnetic field lines entering the stator slot is much smaller than the depth of the stator slot, the influence of the stator yoke on the distribution of magnetic field lines in the stator slot is ignored. The relative air-gap permeability function of the stator cogging effect can be expressed as [33]:

$$B_r = B_{\text{avg}} * \varepsilon, \tag{9}$$

$$\varepsilon = \frac{g_e}{g_e + g_c(\theta)},\tag{10}$$

where  $\varepsilon$  is a function of  $\theta$ ,  $g_c(\theta)$  is the magnetic field line length function with the rotor angle caused by stator slotting, and the distribution of magnetic field lines of the stator tooth is shown in Fig. 16.

Therefore,  $g_c(\theta)$  can be expressed as:

$$g_c(\theta) = \begin{cases} 0 & 0 \le \theta \le \theta_{s1} \\ \frac{\pi}{2} r_d * (\theta - \theta_{s1}) & \theta_{s1} \le \theta \le \theta_{s2} \end{cases}, \tag{11}$$

where  $r_d$  is the radius of the closed integral path circle.

In the form of a Fourier series expansion, it can be expressed as:

$$\varepsilon = \varepsilon_0 + \sum_{j=1,2,3...} \varepsilon_j \cos(jQ_s\theta), \tag{12}$$

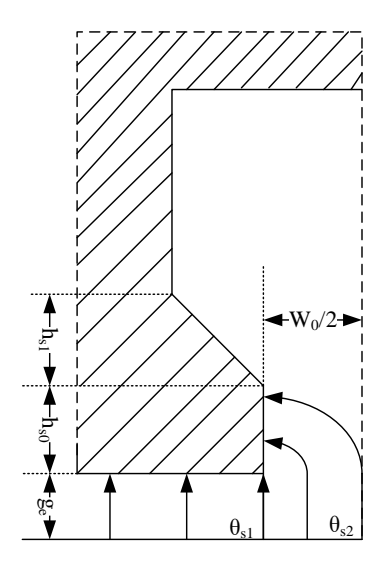


Fig. 16. Schematic diagram of stator slot magnetic field lines

where

$$\varepsilon_0 = \varepsilon_{\text{max}} - \frac{(\varepsilon_{\text{max}} - \varepsilon_{\text{min}}) * (\theta_{s2} - \theta_{s1})}{2\pi/Q_s},$$
(13)

$$\varepsilon_{0} = \varepsilon_{\text{max}} - \frac{(\varepsilon_{\text{max}} - \varepsilon_{\text{min}}) * (\theta_{s2} - \theta_{s1})}{2\pi/Q_{s}},$$

$$\varepsilon_{j} = \frac{4(\varepsilon_{\text{max}} - \varepsilon_{\text{min}})r_{s}}{\pi Q_{s} j^{2}(\theta_{s2} - \theta_{s1})} \left(\cos\left(jQ_{s} \frac{\theta_{s2} - \theta_{s1}}{2r_{s}}\right) - 1\right),$$
(13)

and  $r_s$  is the inter radius of the stator.

The graph of the change of the Carter Factor with the rotor angle under the pole pair was obtained by using MATLAB to calculate as shown in Fig. 17.

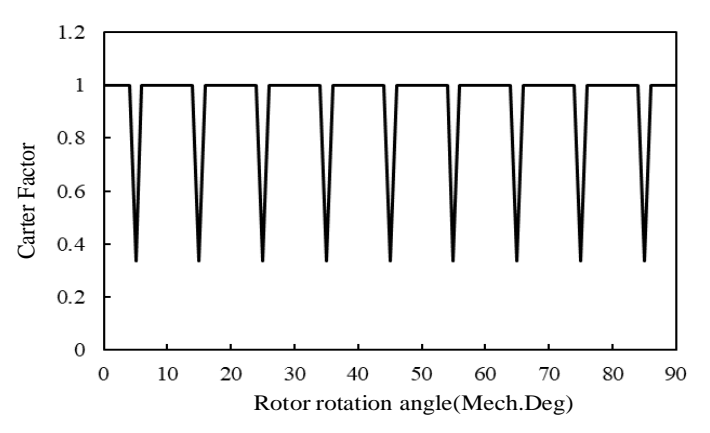


Fig. 17. Carter factor under one pole pair

By combining Eq. (7), (8), (9) and (12), the Fourier expansion formula of the air-gap magnetic density  $B_r(\theta)$  considering the cogging effect of the stator is as follows:

$$B_{r}(\theta) = B_{\text{avg}}(\theta) * \varepsilon$$

$$= \sum_{\nu=1,2,3...} B_{\nu} \cos(\nu p \theta) * \left[ \varepsilon_{0} + \sum_{j=1,2,3...} \varepsilon_{j} \cos(j Q_{s} \theta) \right]$$

$$= \varepsilon_{0} * \sum_{\nu=1,2,3...} B_{\nu} \cos(\nu p \theta) + \sum_{\nu=1,2,3...} \sum_{j=1,2,3...} \frac{1}{2} B_{\nu} \varepsilon_{j} \cos \left[ \left( \nu \mp j \frac{Q_{s}}{p} \right) p \theta \right]. \quad (15)$$

According to Eq. 15, under the modulation of the stator and rotor, the air gap magnetic density will generate a series of harmonics, which can be summarized as: $|vp + jQ_s|$ ,  $(v = 1, 3, 5...; j = 0, \pm 1, \pm 2, \pm 3...)$ . Therefore, the number of harmonic pole pairs and the harmonic rotational velocity can be obtained:

$$P_{(v,j)} = |4v + 36j|, (16)$$

$$\omega_{(v,j)} = \frac{4v\omega}{(4v + 36j)}. (17)$$

The effective number of operating waves and the corresponding rotational velocity of the RSPMSM at 8/36 slots can be deduced, as shown in Table 3.

According to Table 3, the effective harmonic order of the RSPMSM with 8/36 slots are mainly 4, 8, 12, 16, 20, 24, 28, and 32. Among them, 4, 12, 20, and 28 waves are generated by the permanent magnet on the rotor, so the rotational velocity is the same as the rotor. The 8, 16, 24, and 32 waves are all generated by dynamic modulation of the stator and rotor.

Number	Effective harmonic order	Velocity
1	$P_{(1,0)} = 4$	$\omega_{(1,0)} = \omega$
2	$P_{(7,-1)} = 8$	$\omega_{(7,-1)} = -7\omega/2$
3	$P_{(3,0)} = 12$	$\omega_{(3,0)} = \omega$
4	$P_{(5,-1)} = 16$	$\omega_{(5,-1)} = -5\omega/4$
5	$P_{(5,0)} = 20$	$\omega_{(5,0)} = \omega$
6	$P_{(3,-1)} = 24$	$\omega_{(3,-1)} = -\omega/2$
7	$P_{(7,0)} = 28$	$\omega_{(7,0)} = \omega$
8	$P_{(1,-1)} = 32$	$\omega_{(1,-1)} = -\omega/8$

Table 3. Effective harmonic order and velocity of RSPMSM at 8/36 slots

According to Eq. (15), the radial air gap magnetic density waveform and harmonic spectrogram of RSPMSM I at no-load can be obtained, as shown in Fig. 18. From the comparison of the finite element simulation results and the analytical method, it can be seen that the analytical method and the finite element results are in good agreement. The change of the curve is consistent, which

proves the correctness of the analytical method. The data is slightly inconsistent, because the influence of the core saturation in the motor is ignored. In addition, the slotting effect weakens the amplitudes of open-circuit air-gap field near the slot opening.

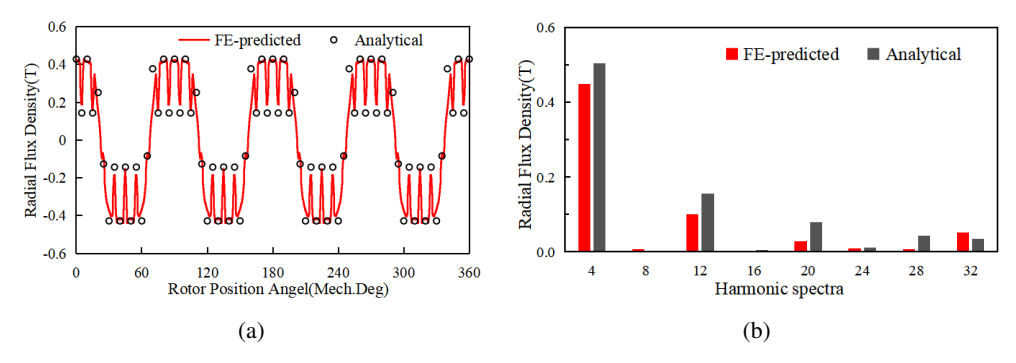


Fig. 18. Radial flux density of RSPMSM I: (a) waveforms; (b) spectra

In Fig. 18(a), the radial air-gap magnetic density waveform undergoes 9 sudden changes towards the origin of the coordinate under pair of magnetic poles, which is the effect of stator slots, corresponding to the structure of the 8/36 slots of the RSPMSM.

In the same way, it can be obtained that the air-gap magnetic density under a pair of magnetic poles of RSPMSM II, without considering the influence of parallel magnetic barriers on both sides of the d-axis magnetic circuit, is shown in Fig. 19. It is a symmetric flat top wave, that is the same as RSPMSM I.

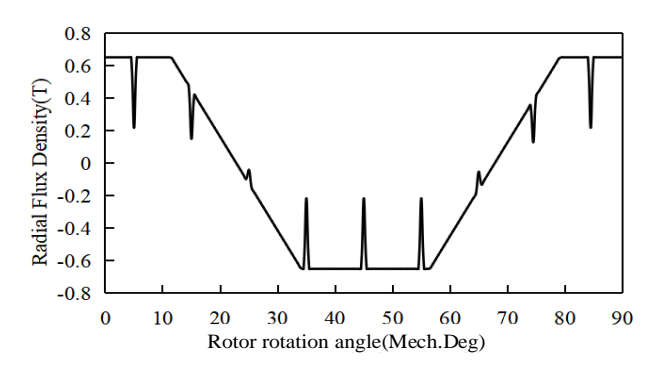


Fig. 19. Radial flux density of RSPMSM II when ignoring parallel magnetic barriers

The magnetic flux tends to flow to the place where the reluctance is small, and the distribution of magnetic field lines will be changed, because RSPMSM II adds a parallel magnetic barrier near the permanent magnet, compared with RSPMSM I, the magnetic field lines at the air magnetic barrier become sparse, and the magnetic field lines at the magnetic bridge are dense, forming a magnetic cohesion effect. Therefore, it is necessary to correct the air gap magnetic density in the parallel magnetic barrier area. The correction coefficients for the three sections are set as follows:  $\alpha_1$ ,  $\alpha_2$  and  $\alpha_3$ . The range to be corrected is determined by the position angle of the three parallel

magnetic barriers. The correction factor can be given by:

$$\alpha_i = \frac{B'_{ri}}{B_{ri}},\tag{18}$$

where  $B'_{ri}$  is the result obtained from finite element simulation, and  $B_{ri}$  is the magnetic density obtained by analysis without considering parallel magnetic barriers.

The corrected magnetic-dense waveform and harmonic spectrogram are shown in Fig. 20. The difference between the waveforms of the two results is small, the degree of agreement is high, and the harmonic components are also more consistent. Comparing the radial flux density of RSPMSM I with RSPMSM II, it is found that the error of RSPMSM II is smaller, which indicates that Eq. (18) has a good corrective effect. In Fig. 20(b), the air-gap magnetic density at no-load mainly includes fundamentals, 12, 20, 28, and 32 harmonics of RSPMSM I and RSPMSM II, which is consistent with the results of Table 3 obtained by analytical derivation. The analytical results agree well with the finite element results. This shows that the accuracy of the proposed hybrid MEC method and the equivalent reluctance method have high accuracy, proving the effectiveness of the no-load air-gap reluctance model derived by the method.

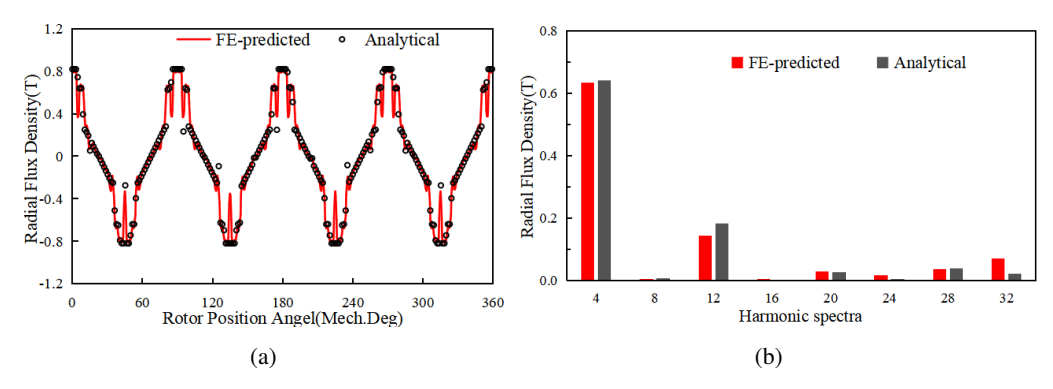


Fig. 20. Radial flux density of RSPMSM II: (a) waveforms; (b) spectra

### 4.2. Quantitative analysis of air-gap field harmonics torque contributions

According to the Maxwell stress tensor method, the tangential electromagnetic force wave expression at any point on the circumference of the air gap is [34]:

$$f_t = \frac{B_r(\theta) * B_t(\theta)}{\mu_0}. (19)$$

The tangential force can be integrated along the selected path to integrate the circumference of the machine to obtain the electromagnetic torque. But a stable torque can only be produced if the radial and tangential air-gap flux density harmonics have the same order and their spatial phase angle difference does not change with time. Therefore, the instantaneous electromagnetic torque

of the RSPMSM can be calculated by:

$$T_{em} = \frac{L_{ar}}{\mu_0} \oint \Upsilon B_r(\theta) B_t(\theta) d\theta = \frac{L_{ar} \Upsilon^2}{\mu_0} \int_0^{2\pi} B_r(\theta) B_t(\theta) d\theta$$
$$= \frac{\pi L_{ar} \Upsilon^2}{\mu_0} \sum_k B_{rk}(\theta) B_{tk}(\theta) \cos(\theta_{rk} - \theta_{tk}) = \sum_k^{\infty} T_k, \tag{20}$$

where  $\Upsilon$  is the radius of the integral path, the radius of any circumference in the air gap,  $B_{rk}$  and  $B_{tk}$  are the k-th Fourier coefficients of the radial and tangential air-gap magnetic flux densities,  $\theta_{rk}$  and  $\theta_{tk}$  are the corresponding phase angles,  $T_k$  is the electromagnetic torque generated by the k-th air-gap magneto-dense harmonics.

Through finite element simulation, the radial and tangential air-gap magnetic dense waveforms and harmonic spectra of RSPMSM I and RSPMSM II at rated load can be obtained, as shown in Fig. 21 and Fig. 22. Compared with the air-gap magnetic density at no-load, it can be seen that due to there is only one excitation source of PM at no-load, and the current winding is added as an excitation source at rated load, the fundamental wave,  $3Q_r$ ,  $5Q_r$ , and  $Q_s - Q_r$  subharmonic amplitude of the air-gap magnetic density is larger at rated load. The magnetic leakage area is saturated at rated load, and the magnetic flux leakage between the poles is suppressed, which will further increase the magnetic density of the air gap. Through the harmonic spectrogram, it can be seen that the effective harmonic is consistent with the analysis results, and the main effective harmonic orders are consistent with the analysis results, which proves the correctness of the analysis. Table 4 shows the magnitude and corresponding phase angles of the tangential and radial air-gap magnetic densities of the two RSPMSMs obtained by Fourier decomposition of  $B_r$  and  $B_t$ .

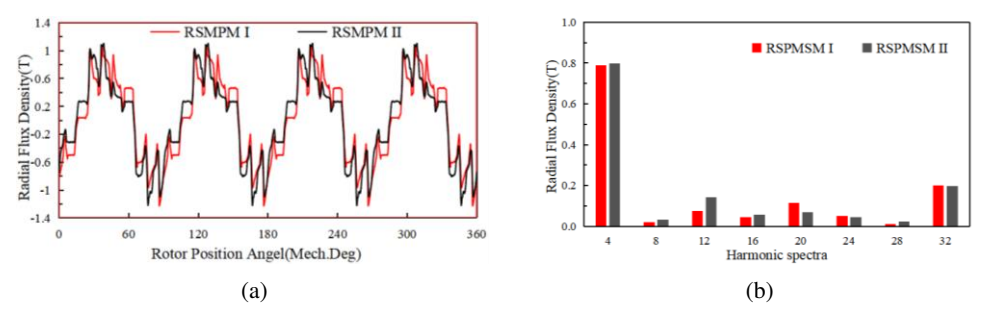
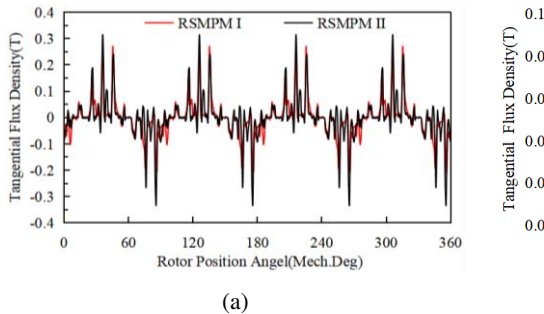


Fig. 21. Radial flux density of two RSMPM machines at rated load: (a) waveforms; (b) spectra

The torque curve of the two RSMPMs of  $I_{\rm rms}$  is shown in Fig. 23. The V-shaped PMs in the RSPMSM II make it easier for the magnetic field lines to pass through the air gap and couple with the stator, while the RSPMSM I has a larger magnetic flux leakage. In terms of torque, the torque of RSPMSM II is greater than that of RSPMSM I at the same current. Figure 24 shows the torque results at rated load of RSPMSM I and RSPMSM II simulated by finite element simulation. The torque of RSPMSM I is 15.9 Nm and that of RSPMSM II is 17.7 Nm. In comparison, the torque of RSPMSM I is smaller, indicating that its load capacity is smaller, but its torque ripple is also smaller, only 7.72%, while the torque ripple of RSPMSM II reaches 15.25%.



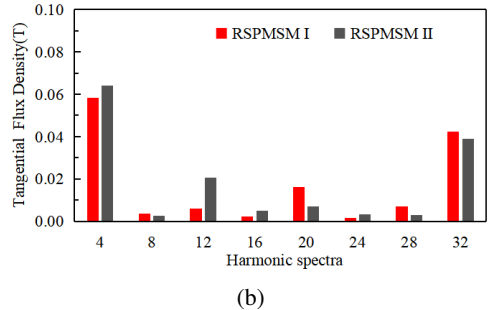
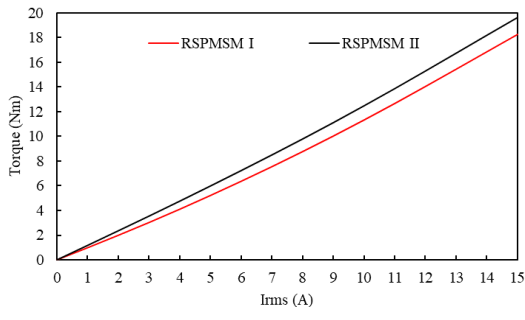


Fig. 22. Tangential flux density of two RSMPM machines at rated load: (a) waveforms; (b) spectra

Table 4. Radial and tangential flux density of two motors

Harmonic order	RSPMSM I			RSPMSM II		
	$B_r(T)$	$B_t$ (T)	$\theta_{rk} - \theta_{tk}$	$B_r(T)$	$B_t$ (T)	$\theta_{rk} - \theta_{tk}$
$Q_r$ (4)	0.7883	0.0585	17.83	0.7973	0.0641	2.31
$3Q_r$ (12)	0.0757	0.0058	179.76	0.1426	0.0206	248.92
$Q_s - 5Q_r (16)$	0.0454	0.0022	209.60	0.0556	0.0048	92.86
$5Q_r$ (20)	0.1134	0.0163	279.74	0.0697	0.0071	350.89
$Q_s - 3Q_r (24)$	0.0518	0.0014	261.65	0.0432	0.0031	288.86
$Q_s - Q_r (32)$	0.2011	0.0424	96.29	0.1971	0.0191	92.85



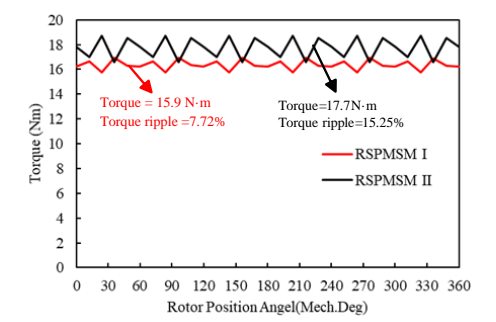


Fig. 23. Variation curve of torques with  $I_{rms}$ 

Fig. 24. Torques of two RSPMSMs at rated load

The torque components to be analyzed by bringing the data from Table 4 into (20), and the torque components and proportions provided by each harmonic order are shown in Table 5.

The proportion of torque contributed by the fundamental wave and the modulated wave of each order can be expressed as:

$$\lambda = \frac{T_k}{T_{AV}} \times 100\%. \tag{21}$$

RSPMSM I RSPMSM II Harmonic **Torque Torque Torque Torque** order contribution proportion contribution proportion (Nm) (%) (Nm) (%) 19.8744 112.35 17.0713 107.37  $TQ_r$  (4)  $T_3Q_r$  (12) -0.1709-1.07-0.4113-2.32 $TQ_s - 5Q_r$  (16) -0.0338 -0.0052 -0.03-0.210.1902  $T5Q_r$  (20) 0.1217 0.77 1.08  $TQ_s - 3Q_r (24)$ -0.0042-0.030.01685 0.10  $TQ_s - Q_r$  (32) -0.3638-2.29-0.1490-0.84FE-predicted 15.9 Nm 17.7 Nm

Table 5. Contribution of each order harmonic in torque

Table 4 and Table 5 show that there are a large number of harmonics in RSPMSM I and RSPMSM II indicating the presence of air gap magnetic field modulation effect, but the torque provided by the fundamental wave is the largest. The torque components provided by the other  $3Q_r$ ,  $Q_s - 5Q_r$ ,  $5Q_r$ ,  $Q_s - 3Q_r$  and  $Q_s - Q_r$  harmonics are much smaller than those of the fundamental wave, and the  $3Q_r$ ,  $Q_s - 5Q_r$  and  $Q_s - Q_r$  harmonics provide negative torque. The detailed contribution and proportion of each harmonic to the torque are shown in Fig. 25. Since the radial and tangential air-gap magnetic dense fundamental waves of RSPMSM I are smaller than those of RSPMSM II, its fundamental contributes a lower torque component, and thus the total resultant torque of RSPMSM I is lower. The results of Fig. 25 are on the larger side compared to Fig. 23, which is due to Fig. 23 shows the results obtained by Maxwell, which is the simulation result of the average electromagnetic torque. Figure 25 shows the torque components provided by each harmonic calculated by the analytical method, which is the ideal calculated value. According to the Maxwell stress tensor method, the torque is affected by the integration path, when different

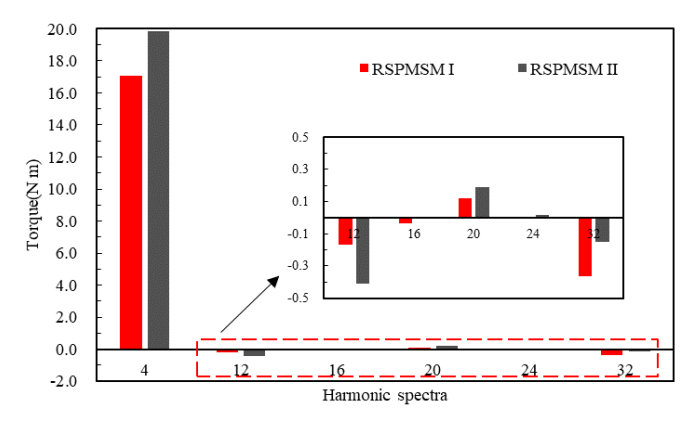


Fig. 25. Contributed torque components of various working harmonics

integration paths are selected, there are differences in the radial and tangential magnetic density components and their phase angles, resulting in errors in the calculated values [35]. But it has no effect on the conclusion that the electromagnetic torque is mainly provided by the fundamental wave, and the contribution of other subharmonics is not large.

### 5. Conclusions

In this paper, the torque generation mechanism of RSPMSM is analyzed. The magnetic equivalent circuit and the equivalent reluctance of different magnetic circuits are used to determine the slotless air-gap magnetism, combined with the influence of the slotted Carter factor, the model of the air-gap magnetism at no load is derived, and the electromagnetic torque generation mechanism is analyzed and proved by using the Maxwell stress method. Compared with the finite element analysis and the measured results of the prototype, the following conclusions are drawn.

- It is found that the change of the rotor structure of the two RSPMSMs cannot change the
  main harmonic order of the air gap magnetic flux density, but it can affect the magnitude
  of the fundamental wave and each harmonic, and affect the torque contribution of each
  harmonic. Moreover, the torque components provided by the other minor harmonics are
  smaller than the fundamental wave.
- The torque contribution of the air gap magnetic field modulation harmonic is positive and negative, so the torque component of the total harmonic contribution of the magnetic field modulation is low.
- 3. Since the radial and tangential air-gap magnetic density fundamental of RSPMSM I is smaller than that of RSPMSM II, its fundamental contribution is lower, so the total combined torque of RSPMSM I is lower but the torque ripple is also lower.
- 4. The demagnetization stability of RSPMSM I is consistently higher than that of RSPMSM II under both rated and weak magnetic field conditions.

### Acknowledgements

This work was supported by National Natural Science Foundation of China Grant No. 52067008, in part by Jiangxi Provincial Key Laboratory of Multidimensional Intelligent Perception and Control under No. 2024SSY03161, and in part by Jiangxi Natural Science Foundation Youth Project under 20242BAB20219.

### References

- [1] Wei F., Zhu Z., Qu H., Yan L., Qi J., New dual-PM spoke-type flux-reversal machines for direct-drive applications, IEEE Transactions on Industry Applications, vol. 58, no. 5, pp. 6190–6202 (2022), DOI: 10.1109/TIA.2022.3190248.
- [2] Zhang L., Han S., Zhu X., Quan L., Chen W., Research on five-phase flux-intensifying permanent magnet motor drive system based on new active sensorless strategy, IEEE Transactions on Transportation Electrification, vol. 9, no. 3, pp. 4266–4277 (2023), DOI: 10.1109/TTE.2023.3241089.
- [3] Wei F., Zhu Z., Yan L., Qi J., *Investigation of stator/rotor pole number combinations and PM numbers in consequent-pole hybrid excited flux reversal machine*, IEEE Transactions on Energy Conversion, vol. 37, no. 3, pp. 2092–2106 (2022), DOI: 10.1109/TEC.2022.3163654.

- [4] Liu X., Liu D., Zhu S., Liang J., *Investigation of an intensifying-flux variable flux-leakage interior permanent magnet machine for wide speed range*, CES Transactions on Electrical Machines and Systems, vol. 6, no. 2, pp. 207–215 (2022), DOI: 10.30941/CESTEMS.2022.00028.
- [5] Cao L., Zuo Y., Xie S., Hoang C., Han B., Lee C., Comparative study of permanent-magnet vernier motor and interior permanent-magnet motor for hybrid electric vehicles, IEEE Transactions on Industry Applications, vol. 59, no. 6, pp. 6601–6614 (2023), DOI: 10.1109/TIA.2023.3292813.
- [6] Mao J., Huang J., Xu X., Zheng J., Zhang X., Design and analysis of interior permanent magnet motor with magnetic isolation and heat dissipation integrated auxiliary slot, IEEE Access, vol. 11, pp. 93004–93011(2023), DOI: 10.1109/ACCESS.2023.3309421.
- [7] Lim D., Yi K., Woo D., Yeo H., Ro J., Lee C., *Analysis and design of a multi-layered and multi-segmented interior permanent magnet motor by using an analytic method*, IEEE Transactions on Magnetics, vol. 50, no. 6, pp. 1–8 (2014), DOI: 10.1109/TMAG.2013.2296568.
- [8] An Y., Ma C., Zhang N., Guo Y., Degano M., Gerada C., Open-circuit air-gap magnetic field calculation of interior permanent magnet synchronous motor with V-shaped segmented skewed poles using hybrid analytical method, IEEE Transactions on Magnetics, vol. 57, no. 12, pp. 1–9 (2021), DOI: 10.1109/TMAG.2021.3118222.
- [9] Ma C., Zhang J., Wang J., Yang N., Liu Q., Zuo S., Analytical model of open-circuit air-gap field distribution in interior permanent magnet machines based on magnetic equivalent circuit method and boundary conditions of macroscopic equations, IEEE Transactions on Magnetics, vol. 57, no. 3, pp. 1–9 (2021), DOI: 10.1109/TMAG.2021.3051498.
- [10] Qu R., Lipo T., Analysis and modeling of air-gap and zigzag leakage fluxes in a surface-mounted permanent-magnet machine, IEEE Transactions on Industry Applications, vol. 40, no. 1, pp. 121–127 (2004), DOI: 10.1109/TIA.2003.821790.
- [11] Xu L., Zhang C., Zhu X., Lin M., Zheng S., Indirect analytical modeling and analysis of V-shaped interior PM synchronous machine, IEEE Access, vol. 7, pp. 173786–173795 (2019), DOI: 10.1109/AC-CESS.2019.2956764.
- [12] Zhu Z., Howe D., Bolte E., Ackermann B., *Instantaneous magnetic field distribution in brushless permanent magnet DC motors. I. Open-circuit field*, IEEE Transactions on Magnetics, vol. 29, no. 1, pp. 124–135 (1993), DOI: 10.1109/20.195557.
- [13] Dianati B., Hahn I., Nonlinear modeling of MGSPMs based on hybrid subdomain and magnetic equivalent circuitry, IEEE Transactions on Magnetics, vol. 58, no. 1, pp. 1–10 (2022), DOI: 10.1109/TMAG.2021.3128739.
- [14] Li Z., Huang X., Chen Z., Wu L., Shen Y., Shi T., *Electromagnetic analysis for interior permanent-magnet machine using hybrid subdomain model*, IEEE Transactions on Energy Conversion, vol. 37, no. 2, pp. 1223–1232 (2022), DOI: 10.1109/TEC.2021.3112813.
- [15] Ladghem Chikouche B., Boughrara K., Dubas F., *Two-dimensional hybrid model for magnetic field calculation in electrical machines: exact subdomain technique and magnetic equivalent circuit*, The International Journal for Computation and Mathematics in Electrical and Electronic Engineering, vol. 40, no. 3, pp. 535–560 (2021), DOI: 10.1108/COMPEL-01-2021-0008.
- [16] Ullah W., Khan F., Sulaiman E., Sami I., Ro J., Analytical sub-domain model for magnetic field computation in segmented permanent magnet switched flux consequent pole machine, IEEE Access, vol. 9, pp. 3774–3783 (2021), DOI: 10.1109/ACCESS.2020.3047742.
- [17] Lee S., Kim C., Choo Y., Yun G., Lee C., *Torque analysis of a permanent magnet synchronous motor using flux densities in air gap*, AIP Advances, vol. 13, no. 2, 025313 (2023), DOI: 10.1063/9.0000566.

- [18] Li Y., Zhou Q., Ding S., Li W., Hang J., *Investigation of air-gap field modulation effect in spoke-type PM machines*, IEEE Transactions on Transportation Electrification, vol. 9, no. 1, pp. 845–855 (2023), DOI: 10.1109/TTE.2022.3202042.
- [19] Li Y., Zhou Q., Ding S., Li W., Hang J., Design and evaluation of reduced-rare-earth interior consequent-pole permanent magnet machines for automotive applications, IEEE Transactions on Industry Applications, vol. 59, no. 2, pp. 1372–1382 (2023), DOI: 10.1109/TIA.2022.3184665.
- [20] McFarland J., Jahns T., EL-Refaie A., Analysis of the torque production mechanism for flux-switching permanent-magnet machines, IEEE Transactions on Industry Applications, vol. 51, no. 4, pp. 3041–3049 (2015), DOI: 10.1109/TIA.2015.2411655.
- [21] Guo F., Chu Q., Li C., *Torque analysis and stator windings influence research on negative-salient permanent magnet synchronous motor*, 2022 2nd International Joint Conference on Energy and Environmental Engineering, vol. 9, no. 2, pp. 416–424 (2023), DOI: org/10.1016/j.egyr.2023.03.015.
- [22] Zhu X., Huang J., Quan L., Xiang Z., Shi B., *Comprehensive sensitivity analysis and multiobjective optimization research of permanent magnet flux-intensifying motors*, IEEE Transactions on Industrial Electronics, vol. 66, no. 4, pp. 2613–2627 (2019), DOI: 10.1109/TIE.2018.2849961.
- [23] Bianchi N., Bolognani S., Chalmers B.J., Salient-rotor PM synchronous motors for an extended flux-weakening operation range, IEEE Trans. Ind., vol. 36, no. 4, pp. 1118–1125 (2000), DOI: 10.1109/28.855968.
- [24] Wang T., Zhu X., Zheng S., Quan L., Xiang Z., Zhou X., Investigation on Torque Characteristic and PM Operation Point of Flux-Intensifying PM Motor Considering Low-Speed Operation, IEEE Transactions on Magnetics, vol. 57, no. 2, pp. 1–5 (2023), DOI: 10.1109/TMAG.2020.3019299.
- [25] Zhu X., Wu W., Yang S., Xiang Z., Quan L., Comparative design and analysis of new type of flux-intensifying interior permanent magnet motors with different q-axis rotor flux barriers, IEEE Transactions on Energy Conversion, vol. 33, no. 4, pp. 2260–2269 (2018), DOI: 10.1109/TEC.2018.2837119.
- [26] Zhu X., Yang S., Du Y., Xiang Z., Xu L., Electromagnetic performance analysis and verification of a new flux-intensifying permanent magnet brushless Motor with two-layer segmented permanent magnets, EEE Transactions on Magnetics, vol. 52, no. 7, pp. 1–4 (2016), DOI: 10.1109/TMAG.2016.2519465.
- [27] Wu W., Chen Q., Zhu X., Design and analysis of a new permeability-modulated interior permanent-magnet synchronous machine, IEEE Transactions on Magnetics, vol. 57, no. 2, pp. 1–5 (2021), DOI: 10.1109/TMAG.2020.3015784.
- [28] Liu X., Zhu S., Liu D., Liang J., *Design and analysis of wide speed regulation of variable leakage flux reverse salient-pole motor*, CES Transactions on Electrical Machines and Systems, vol. 7, no. 3, pp. 284–293 (2023), DOI: 10.30941/CESTEMS.2023.00031.
- [29] Liu X., Liu D., Zhu S., *Investigation of an intensifying-flux variable flux-leakage interior permanent magnet machine for wide speed range*, CES Transactions on Electrical Machines and Systems, vol. 6, no. 2, pp. 207–215 (2022), DOI: 10.30941/CESTEMS.2022.00028.
- [30] Qiu H., Zhang S., *Rotor optimization of axial-radial flux type synchronous machine based on magnetic flux leakage*, Archives of Electrical Engineering, vol. 70, no. 3, pp. 551–566 (2021), DOI: 10.24425/aee.2021.137573.
- [31] Xu H., Kamada H., Nomura S., A simple calculation method for center magnetic flux density of a magnetic core electromagnet with a wide air gap, IEEE Transactions on Applied Superconductivity, vol. 32, no. 6, pp. 1–6 (2022), DOI: 10.1109/TASC.2022.3158350.
- [32] Abdelkefi A., Souissi A., Abdhennader I., Analytical investigation of flux switching PM machines: air gap flux density formulation, 2022 Second International Conference on Sustainable Mobility Applications, Renewables and Technology (SMART), pp. 23–25 (2022), DOI: 10.1109/SMART55236.2022.9990436.

- [33] Seo J., Choi H., Cogging torque calculation for IPM having single layer based on magnetic circuit model, IEEE Transactions on Magnetics, vol. 50, no. 10, pp. 1–4 (2014), DOI: 10.1109/TMAG.2014.2327204.
- [34] Zhu W., Pekarek S., Fahimi B., Deken B., *Investigation of force generation in a permanent magnet synchronous machine*, IEEE Transactions on Energy Conversion, vol. 22, no. 3, pp. 557–565 (2007), DOI: 10.1109/TEC.2006.888034.
- [35] Shi Z., Rajanathan C., A new method to improve the accuracy of Maxwell stress based force calculation in computational electromagnetic fields, 1996 Third International Conference on Computation in Electromagnetics, pp. 241–246 (1996), DOI: 10.1049/cp:19960192.